PNAS
www.pnas.org

Supplementary Information for

Hippocampus-Dependent Emergence of Spatial Sequence Coding in Retrosplenial Cortex

Dun Mao, Adam R. Neumann, Jianjun Sun, Vincent Bonin, Majid H. Mohajerani, and Bruce L. McNaughton

Correspondence: zjumao@gmail.com (D.M.), bruce.mcnaughton@uleth.ca (B.L.M).

This PDF file includes:

www.pnas.org/cgi/doi/10.1073/pnas.1803224115

Methods

Animals and surgery. All animal procedures were performed in compliance with protocols approved by the ethical research committee of the University of Lethbridge. Fifteen adult male and female transgenic GCaMP6 mice (20-25 g, 2-4 months old at the time of surgery, including 13 Thy1 GCaMP6s GP4.3 mice (1, 2) and 2 Ai93 (TITL-GCaMP6f) || CaMK2a-tTA || Rasgrf2-2A-dCre mice (3)) were used in this study. Although it is not the case in this study, there is one recent paper reporting epileptiform events in Ai93 mouse with certain Cre drivers (4). The Thy1 GCaMP6s GP4.3 mouse line was used due to its stable, homogeneous expression over a large population of cortical excitatory neurons. It has also been used to study several other cortical areas, including the mouse visual and motor cortices (5, 6). Mice were divided into 3 experimental groups, sham lesion (control, n = 5 Thy1 mice), unilateral hippocampal lesion (uni-lesion, n = 3 Thy1 mice and n = 2 Ai93 mice), bilateral hippocampal lesions (bi-lesion, n = 5 Thy1 mice). Mice were injected with dexamethasone (0.2 mg/kg, intramuscular), 0.5 mL 5% dextrose and 0.9% saline solution mixed with atropine (3 µg/mL, subcutaneous) and phenobarbital (30 mg/kg, subcutaneous) before surgery. Mice were anesthetized with isoflurane (4% induction, 1.5% maintenance) and body temperature was maintained at 37°C using a closed-loop system. A custom-made titanium head plate (7) was attached to the skull using dental cement and acrylic material. A ~3 mm bilateral craniotomy was made (1.5 mm lateral of the midline for each hemisphere, 2 mm anterior and 1 mm posterior of lambda). The craniotomy was rinsed and covered with brain buffer right after bone removal.

Excitotoxic hippocampal lesions (15 mg/mL, NMDA in 1x phosphate-buffered saline) were made in the 2 lesion groups. Injections were made with a micropipette loaded on a nanoliter injector (Nanoject II, Drummond Sci.). In total 4 injection sites were used: AP -2.3 mm, ML 1.5 mm, DV 1.8 mm in both hemispheres and AP -3.2 mm, ML 2.5 mm, DV 2.0 mm in both hemispheres. Sham lesions were made in the control group (penetration of NMDA-filled micropipette to DV 1.0 mm without injections). For the uni-lesion group, injections of NMDA solution were made in either the left or right hemisphere at the speed of 9.2 nL/pulse for 8 pulses (in total: 9.2 nL/pulse x 8 pulses = 73.6 nL, inter-pulse interval: 15 s) at each site in the selected hemisphere. Sham lesions were made in the other hemisphere (micropipette penetration but no injections). For the bi-lesion group, injections of NMDA solution were made in both hemispheres for the same amount (73.6 nL) at each site. For the uni-lesion and bi-lesion mice, diazepam (5 mg/kg, intraperitoneal) was administered right after surgery to suppress potential seizure behavior due to hippocampal lesions.

A cranial window composed of three round coverslips (diameter: 3 mm x 2 and 5 mm x 1, affixed with optical adhesive) was attached to the skull using tissue adhesive and dental cement (7). The superior sagittal sinus and the anterior portion of the traverse sinuses were visible within

the window. Two rubber rings were attached to the head plate using dental cement to form a well to hold distilled water during imaging. Animals were allowed 1 week of post-surgery recovery before treadmill training started.

Treadmill and training. Mice were introduced to a training treadmill that is different from the experimental treadmill (8, 9). Mice were water-restricted and they were trained to be head-fixed and to move on a treadmill belt (150 cm in length) in a gradual manner. The belt (different from the experimental belt) was made from Velcro material and covered with texture patches. The movement of the belt was guided by 2 light-weight, 3-D printed wheels (5 cm in radius) made from polyamide. An aluminum platform was used to support the belt and mice. The platform was covered with Teflon tape to minimize friction. The movement of the belt was only generated by the force of the mice (no motor was used). A rotation encoder was attached to the shaft of one of the wheels to monitor belt movement. A photoelectric sensor was mounted to monitor a fixed location (marked with a reflective tape) on the belt and the signal was used to trigger reward delivery (~2.5 µL 10% sucrose water). A magnetic pinch valve was used for reward delivery and was controlled by a microprocessor board (Arduino Uno). Rails and optical breadboards used for the mechanical construction were obtained from Thorlabs. All behavioral signals were acquired and synchronized with imaging via a data acquisition system (Axon Digidata 1322A).

Mice were on water restriction and their body weights were monitored at least twice daily to ensure that the weights were above 85% of their free-feeding weights. Mice were habituated and trained for a gradually increased duration, from 5 minutes on day 1 to 1.5 hours per day over a period of 2-3 weeks. After training, mice were transferred to the experimental treadmill and imaging started.

One dimensional linear track has been extensively used to probe spatial activity in both freely moving (10) and head-restrained rodents (8, 11). Our previous study has shown that hippocampal CA1 neurons in head-fixed mice show spatial selectivity highly resembling that in freely moving animals (9).

2-photon imaging. We used a Bergamo II multiphoton microscopy (Thorlabs) for our 2-photon calcium imaging. A Ti:Sapphire excitation laser (Coherent) was operated at 920 nm (~80-120 mW laser power at the sample). Laser scanning was controlled by galvo and resonant scanners through a 16x lens (NA = 0.8, Nikon). Green fluorescence from GCaMP6 was collected with a GaAsP photomultiplier tube. Images were collected at the rate of ~20 frames per second. Imaging depths were targeted at 100-200 µm in the superficial agranular retrosplenial cortex. Black fabric was sealed around the objective and the head plate to block stray light. Field of view (FOV) was 835 x 835 µm in size, centered at ~AP -2.5 mm and ~ML 0.5 mm. Typically the superior sagittal sinus was visible within the FOV. Imaging was performed in mirrored

hemispheres in blocks as mice ran on the treadmill. Imaging was performed for 2-3 weeks for each mouse with 1 or 2 days' inter-session interval.

Histology. After all imaging sessions were performed, mice were euthanized and perfused with 1x phosphate-buffered saline and brains were post-fixed with 4% paraformaldehyde for 24 hours. Brains were then cryoprotected in 30% sucrose solution (with 0.02% sodium Azide) before sectioning. Brains were sectioned in the coronal plane at 40 µm using a custom vibratome. We used a NanoZoomer scanning microscopy (Hamamatsu Photonics) to acquire images. Images of coronal sections from AP -0.8 mm to AP -3.8 mm were kept for the quantification of hippocampal lesions. We used a standard mouse brain atlas (12) as reference for identifying the boundaries of hippocampal formation, including CA areas, dentate gyrus, and subiculum. For the uni-lesion group, the volume of remaining hippocampal tissue in the lesioned hemisphere was normalized to that in the intact hemisphere. For the bi-lesion group, the volumes of remaining hippocampal tissue in left and right hemispheres were normalized to the volumes of the hippocampus in the left and right hemispheres of a control mouse, respectively**.**

Data analysis. Data were analyzed in MATLAB (The Mathworks). Images were registered and regions of interests (ROIs) were automatically identified using Suite2P (13). ROIs were then visually inspected and manually adjusted. Raw fluorescence signals were estimated for each ROI using all corresponding pixels. Neuropil contamination was approximated and subtracted (2). Then the baseline-subtracted dF/F0 was calculated for each ROI using the average across pixels (14). The dF/F0 time courses were deconvolved to infer spiking rate using the constrained nonnegative matrix factorization (15). Deconvolved data were used for all following analysis.

Place cell analysis. Methods for selecting place cells were described previously (9). The 150 cm linear track was divided into 100 position bins (1.5 cm per bin). For each trial (lap), the deconvolved dF/F0 of each neuron was mapped (summed) onto corresponding position bins. The resulting position-mapped activity was normalized by the occupancy (the time spent) in each bin. The position-mapped activity was then filtered with a Gaussian window (4.5 cm standard deviation). Neurons with an average activity of less than 0.03% were excluded from further analysis. The final position tuning curve was obtained by averaging the position-mapped activity across all trials. Two approaches were implemented in identifying neurons with position-locked activity (i.e. potential place cells).

The first approach was based on the definition of place fields (16, 17). Place cells had to satisfy these criteria: (1) place fields must be a continuous region with 15-120 cm in width, within which the activity magnitude must be above 30% of the difference between the maximum and minimum activity in the position tuning curve; (2) the mean in-field activity must be at least three times larger than the mean out-of-field activity; (3) more than one third of the trials must have peak position-mapped activity fall within the potential place field.

The second approach was based on spatial information (SI) (18). SI was calculated using the following formula:

$$\mathrm{SI} = \sum_{\mathrm{i}=1}^{N} p_i \frac{f_i}{f} \log_2 \frac{f_i}{f}$$

where p_i is the occupancy probability in the *i*-th position bin; f_i is the occupancy-normalized activity in the *i*-th position bin; f is the overall activity (summed f_i over all bins); and *N* is the number of bins (*N* = 100). The deconvolved time courses were circularly shifted by a random interval relative to the position trace. A new SI was calculated. This procedure was repeated for 1000 times and a distribution of shuffled SI was constructed. The original SI was compared against the shuffled SI distribution. If the original SI was greater than 95 percentile of the shuffled SI, the neuron was considered to carry significant spatial information and identified as a potential place cell. As shown in Figure S3, these two measures of place cells were highly correlated. Place field position was defined as the position that elicited the maximum activity in the position tuning curve. Place field width was defined as the consecutive position bins in which the activity was above 20% of the difference between peak and baseline activity from the baseline. Our conservative approaches also identified place cells with more than one place field.

Bayesian decoding. We used a Bayesian algorithm (19) to estimate the probability of position given the activity of all imaged neurons (no place cell selection, all neurons were included). By using this method, we wanted to compensate potential biases in the selection of place cells by different methods. Bayesian decoding was performed for running period where the speed was above 1 cm/s. Odd trials were used for training while even trials were used for testing the model. The size of non-overlapping time bins was selected to minimize decoding errors (0.5 s) (Figure S3A). Bayesian decoding error was defined as the absolute difference between true position and decoded position (position with maximum likelihood given population activity); the median of the decoding error distribution was compared. Detailed algorithm was as following (20), we wanted to estimate the probability of animal's position on the treadmill given all neurons' deconvolved dF/F in a short time window:

$$P\left(pos \middle| \left(\frac{dF}{F}\right)_{all}\right) = \frac{P((dF/F)_{all}|pos) \times P(pos)}{P((dF/F)_{all})}$$

where pos denotes position; $(dF/F)_{all}$ denotes the activity of all imaged neurons; P stands for probability. $P(pos)$ was calculated based on the occupancy in each position bin. Based on the assumption of independent firing rates of all imaged neurons and Poisson distribution of firing rates,

$$P\left(\left(\frac{dF}{F}\right)_{all}\middle|pos\right) = \prod_{i=1}^{N} P\left(\left(\frac{dF}{F}\right)_{i}\middle|pos\right)$$

$$= \prod_{i=1}^{N} \frac{(\tau f_i(pos))^{n_i}}{n_i!} e^{-\tau f_i(pos)}$$

where τ is the size of the time bin; $f_i(pos)$ is the position tuning curve for the i-th neurons (constructed using only odd trials); N is the total number of neurons; n_i is the mean activity of the i-th neuron within the time bin. Thus, we have,

$$P\left(pos\middle|\left(\frac{dF}{F}\right)_{all}\right) = C\left(\prod_{i=1}^{N} f_i(pos)^{n_i}\right) e^{-\tau\sum_{i=1}^{N} f_i(pos)}$$

where C is a normalization factor such that $P\left(pos\middle|\left(\frac{dF}{F}\right)_{all}\right)$ sums to 1. $P\left(pos\middle|\left(\frac{dF}{F}\right)_{all}\right)$ is the probability distribution of position for the current time bin. Position with the maximum probability was considered as the decoded position for the current time bin.

Identification of the same neurons across days. For each mouse, we performed imaging at the same coordinate and depth over time. We further used blood vessel patterns and a few landmarks to find the same FOVs over time. The average image on one day was registered to the average image on another day using phase correlation. Then the ROIs mask images were registered using the obtained transformation parameters. ROIs with at least 60% overlapping were identified as potential same neurons. Each candidate pair then went through visual inspection: only neuron pairs with identical surrounding anatomical structures in the average images were kept for further analysis. We identified such neuron pairs imaged across days in 4 control mice, 3 uni-lesion mice, and 4 bi-lesion mice.

Population vector analysis. The position-mapped activity of all place cells in a session was sorted by the positions that elicited the neurons' peak responses. For each cell, the position-mapped activity was normalized so that it had activity ranged from 0 to 1. The population vector was the activity vector of all place cells in a certain position bin. The population vector correlation was the Pearson's linear correlation coefficient between two population vectors. Population vector correlation of the same position was defined as the correlation between population vectors that were less than 15 cm apart in position.

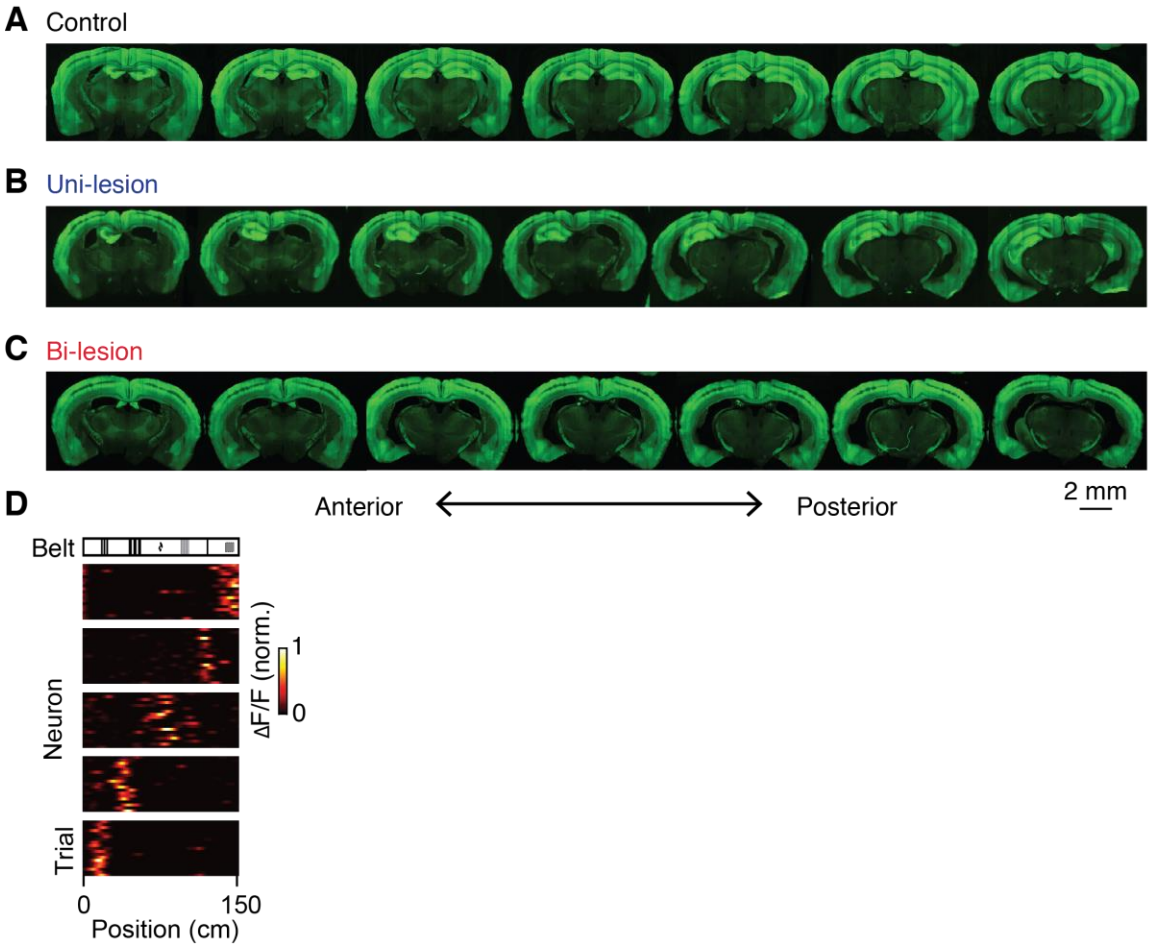

Fig. S1. Example histology and RSC positional activity. (A-C) Example histology of one example mouse from each of the 3 experimental groups. Note the hippocampal tissue loss in the lesion groups, unilateral hippocampal lesion in (B) and bilateral hippocampal lesions in (C). (D) Position activity maps over multiple trials for 5 example RSC place cells from a well-trained control mouse. Belt diagram is shown at the top.

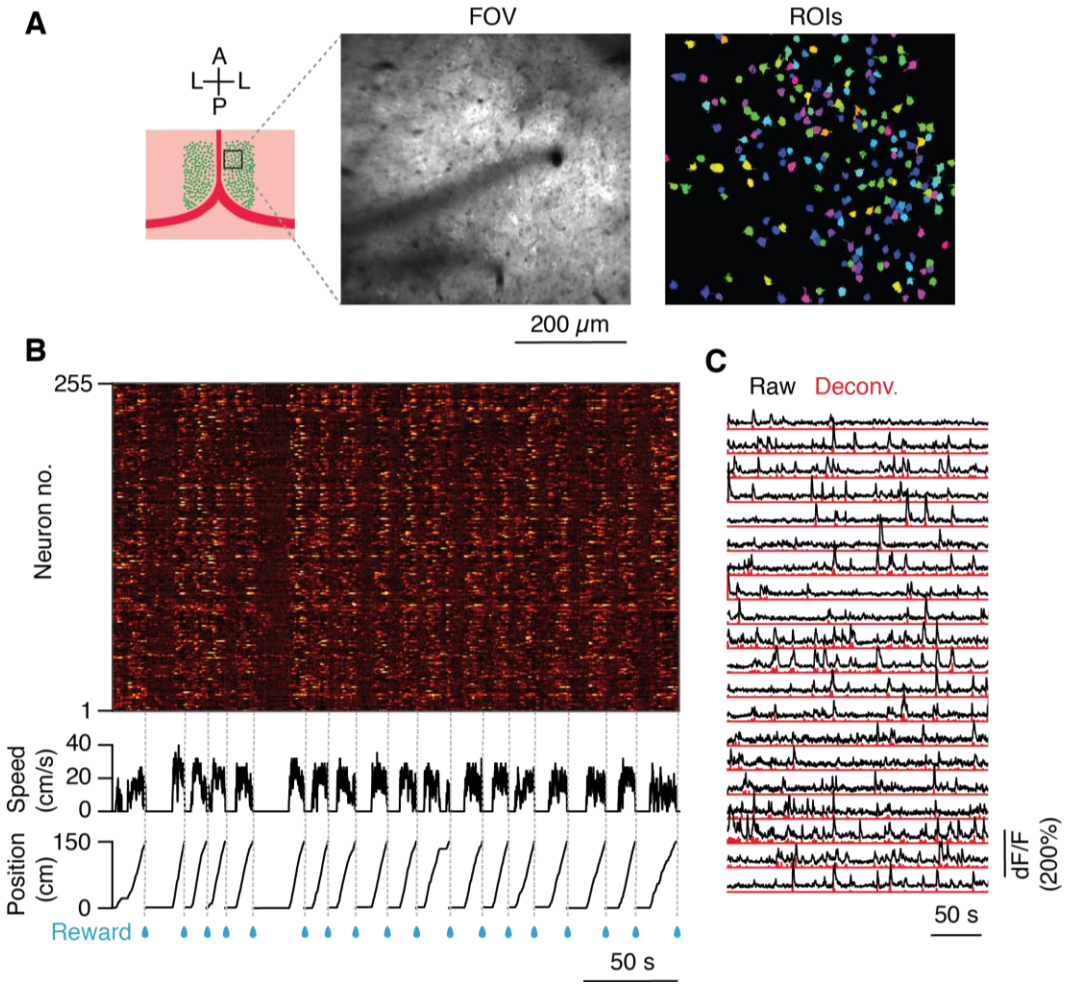

Fig. S2. Example RSC neuronal imaging. (A) RSC imaging diagram (left), example field of view (FOV), and identified regions of interest (ROIs, different colors indicate different neurons). (B) Example colormap plot of the raw calcium time courses of 255 simultaneously imaged neurons at 150 μm depth in dysgranular RSC. Speed and position traces are shown below. Mice were rewarded at 0 cm position (blue drops & dashed lines). (C) Example raw calcium time courses (black traces) and corresponding deconvolved time courses (red traces). The deconvolved data were used for all following analysis.

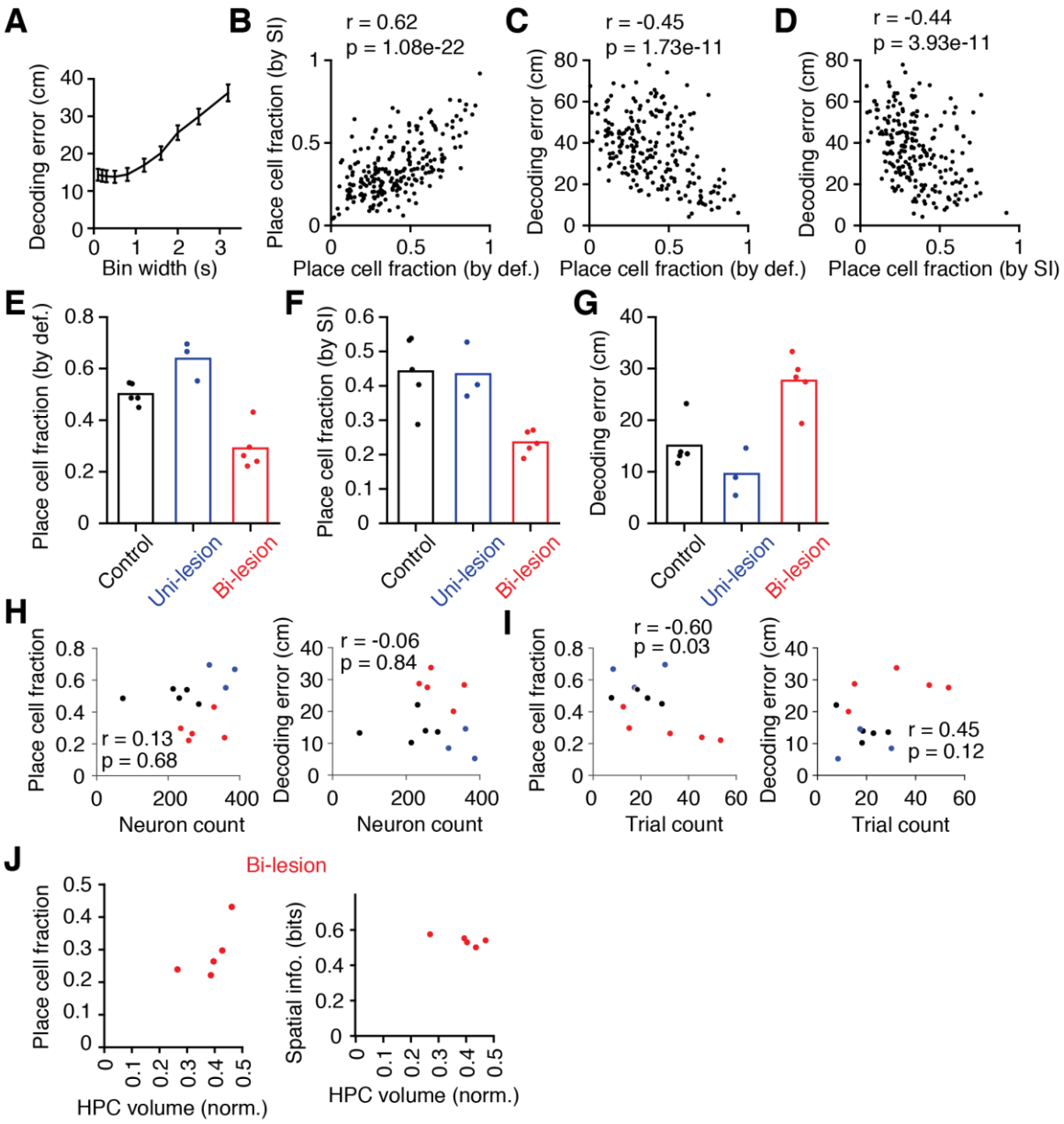

Fig. S3. Different measurements of place cell activity, correlation with other variables. (A) Mean decoding error as a function of bin size. Bin size of 0.5 s was chosen for all following analysis. (B) Scatter plot of the place cell fractions quantified using spatial information (SI) and using definition (def.) for all sessions in the 3 experimental groups. See Methods. (C,D) Scatter plots of the decoding error and place cell fraction quantified using definition (C) and spatial information (D). (E) Bar plot of the average place cell fractions for the 3 experimental groups. Place cells were selected using definition (def.), as shown in (B). Only Thy1 mice were included. (F) The same as (E) but place cells here were selected by spatial information (SI). (G) The same as (E) but for decoding error. (H) Scatter plot of place cell fraction (left) and decoding error (right) as a function of mean neuron count for individual mice. (I) The same as (H) but now the X axis is the mean trial count. (J) Scatter plot of the place cell fraction (left) and spatial information (right) and residual volume (normalized) of the hippocampus for the 5 mice in the bi-lesion group.

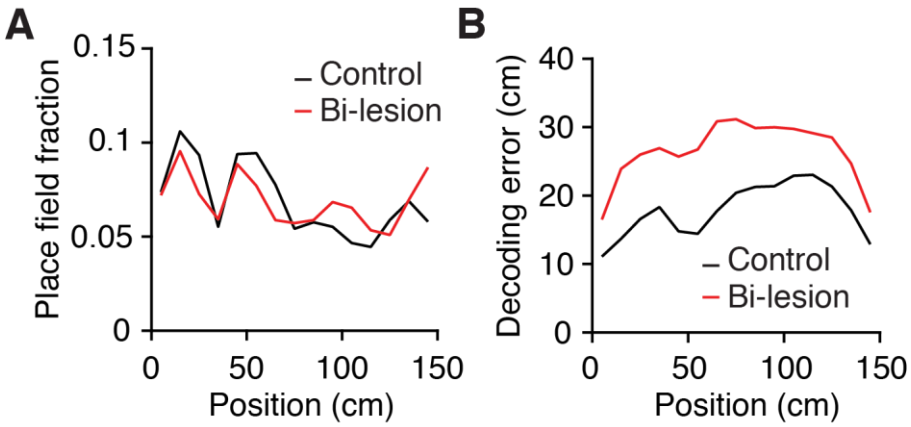

Fig. S4. Place field fraction (A) and decoding error (B) as a function of position for the control animals (black) and bilateral lesion animals (red).

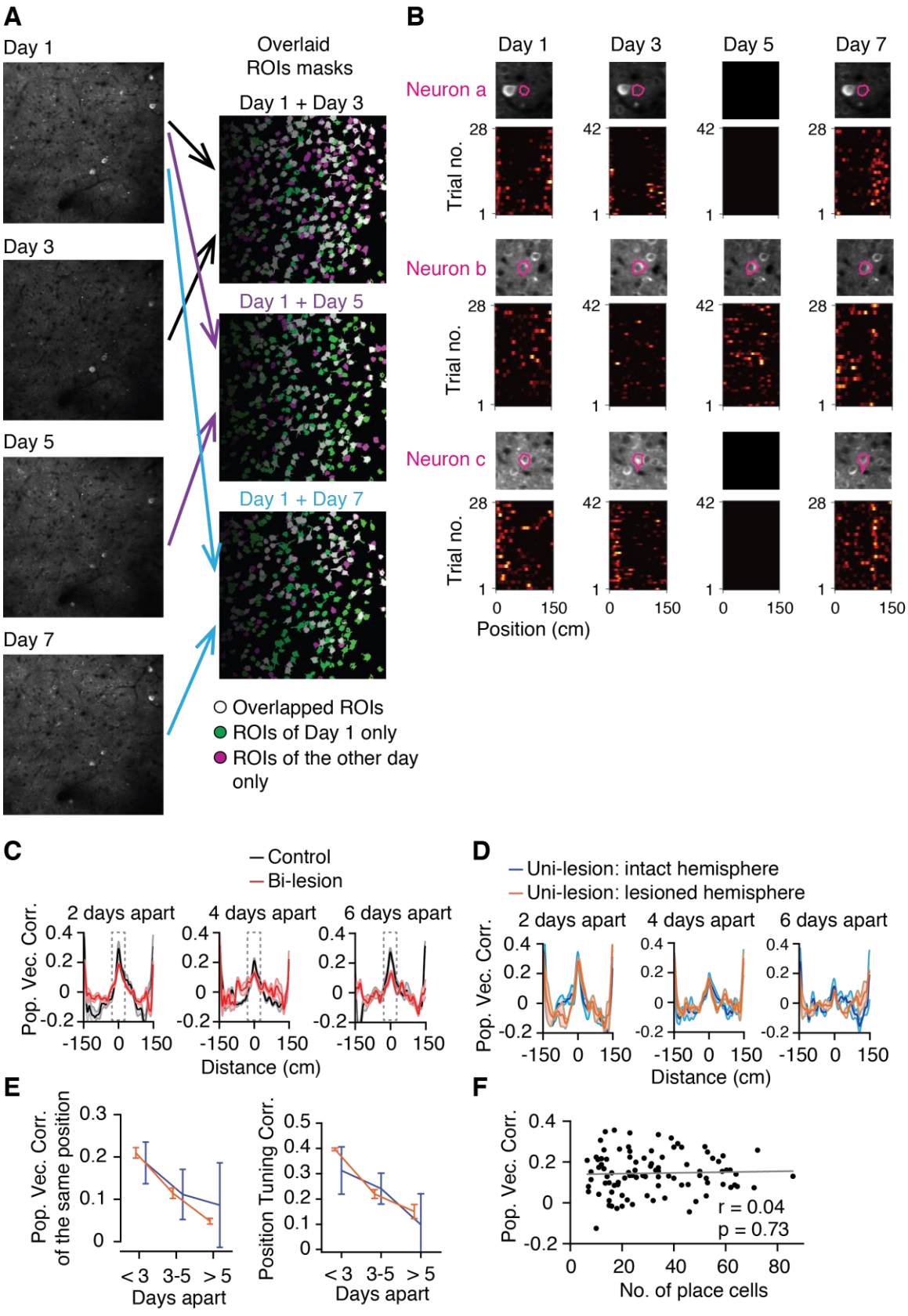
A
Day 1
Day 3
Day 5
Day 7
Overlaid ROIs masks
Day 1 + Day 3
Day 1 + Day 5
Day 1 + Day 7
Overlapped ROIs
ROIs of Day 1 only
ROIs of the other day only
B
Day 1
Day 3
Day 5
Day 7
Neuron a
Neuron b
Neuron c
Trial no.
Position (cm)
C
Control
Bi-lesion
2 days apart
4 days apart
6 days apart
Pop. Vec. Corr.
Distance (cm)
D
Uni-lesion: intact hemisphere
Uni-lesion: lesioned hemisphere
2 days apart
4 days apart
6 days apart
Pop. Vec. Corr.
Distance (cm)
E
Pop. Vec. Corr. of the same position
Days apart
Position Tuning Corr.
Days apart
F
Pop. Vec. Corr.
r = 0.04
p = 0.73
No. of place cells

Fig. S5. RSC place cell activity correlations across days. (A) Left column, mean imaging planes on days 1, 3, 5, 7 in RSC from an example mouse; right column, overlaid ROIs masks between day 1 and other days (see arrows). Overlapped ROIs are indicated as white blobs. ROIs of day 1 only are indicated as green blobs. ROIs of the other day only are indicated by purple blobs. (B) Average images (centered on the outlined neuron, magenta) and position activity maps of 3 example neurons on corresponding days. Black colormaps indicate no activity on that day. (C,D) Population vector correlations (Pop. Vec. Corr.) as a function of distance for position activity maps that were 2 (left), 4 (middle), and 6 (right) days apart for the control and bi-lesion groups (C), and intact and lesioned hemispheres in the uni-lesion group (D). Only neurons identified between days were included in the calculation. Dashed rectangle in (C) indicates area in which distance is within 15 cm. Shaded area: SEM. (E) Left, mean population vector correlations of the same position (distance < 15 cm) as a function of different imaging intervals for the uni-lesion group. Error bars, SEM over animals. Corr., intact side, 0.14 ± 0.05; lesioned side, 0.12 ± 0.01; p = 0.78, two-sample *t*-test. Right, mean position tuning correlations as a function of different imaging intervals for the uni-lesion group. Only neurons identified between days were included in the analysis. Error bars, SEM over animals. Correlation comparison, p = 0.90, two-sample *t*-test. (F) Scatter plot of the population vector correlation as a function of number of place cells. Gray line, linear fit to all dots.

References

1. Dana H, *et al.* (2014) Thy1-GCaMP6 transgenic mice for neuronal population imaging in vivo. *PLoS One* 9(9):e108697.
2. Chen TW, *et al.* (2013) Ultrasensitive fluorescent proteins for imaging neuronal activity. *Nature* 499(7458):295-300.
3. Madisen L, *et al.* (2015) Transgenic mice for intersectional targeting of neural sensors and effectors with high specificity and performance. *Neuron* 85(5):942-958.
4. Steinmetz NA, *et al.* (2017) Aberrant Cortical Activity in Multiple GCaMP6-Expressing Transgenic Mouse Lines. *eNeuro* 4(5).
5. Sun W, Tan Z, Mensh BD, & Ji N (2016) Thalamus provides layer 4 of primary visual cortex with orientation- and direction-tuned inputs. *Nat Neurosci* 19(2):308-315.
6. Chen TW, Li N, Daie K, & Svoboda K (2017) A Map of Anticipatory Activity in Mouse Motor Cortex. *Neuron* 94(4):866-879 e864.
7. Goldey GJ, *et al.* (2014) Removable cranial windows for long-term imaging in awake mice. *Nat Protoc* 9(11):2515-2538.
8. Royer S, *et al.* (2012) Control of timing, rate and bursts of hippocampal place cells by dendritic and somatic inhibition. *Nat Neurosci* 15(5):769-775.
9. Mao D, Kandler S, McNaughton BL, & Bonin V (2017) Sparse orthogonal population representation of spatial context in the retrosplenial cortex. *Nat Commun* 8(1):243.
10. Gothard KM, Skaggs WE, & McNaughton BL (1996) Dynamics of mismatch correction in the hippocampal ensemble code for space: interaction between path integration and environmental cues. *J Neurosci* 16(24):8027-8040.

11. Harvey CD, Collman F, Dombeck DA, & Tank DW (2009) Intracellular dynamics of hippocampal place cells during virtual navigation. *Nature* 461(7266):941-946.
12. Paxinos G & Franklin KBJ (2001) *The Mouse Brain in Stereotaxic Coordinates* (Academic Press) Second edition Ed.
13. Pachitariu M, *et al.* (2016) Suite2p: beyond 10,000 neurons with standard two-photon microscopy. *bioRxiv*.
14. Bonin V, Histed MH, Yurgenson S, & Reid RC (2011) Local diversity and fine-scale organization of receptive fields in mouse visual cortex. *J Neurosci* 31(50):18506-18521.
15. Pnevmatikakis EA, *et al.* (2016) Simultaneous Denoising, Deconvolution, and Demixing of Calcium Imaging Data. *Neuron* 89(2):285-299.
16. Mizuseki K, Royer S, Diba K, & Buzsaki G (2012) Activity dynamics and behavioral correlates of CA3 and CA1 hippocampal pyramidal neurons. *Hippocampus* 22(8):1659-1680.
17. Dombeck DA, Harvey CD, Tian L, Looger LL, & Tank DW (2010) Functional imaging of hippocampal place cells at cellular resolution during virtual navigation. *Nat Neurosci* 13(11):1433-1440.
18. Skaggs WE, McNaughton BL, Gothard KM, & Markus EJ (1993) An information-theoretic approach to deciphering the hippocampal code. *Proceeding Advances in Neural Information Processing Systems*, (Citeseer), pp 1030-1037
19. Zhang K, Ginzburg I, McNaughton BL, & Sejnowski TJ (1998) Interpreting neuronal population activity by reconstruction: unified framework with application to hippocampal place cells. *J Neurophysiol* 79(2):1017-1044.
20. Davidson TJ, Kloosterman F, & Wilson MA (2009) Hippocampal replay of extended experience. *Neuron* 63(4):497-507.